

# Time-varying Excess Earth-glow Backgrounds in the WFC3/IR Channel

G. Brammer, N. Pirzkal, P. McCullough, J. MacKenty

April 8, 2014

---

## ABSTRACT

*We investigate the cause of strong time-dependent variations of the background levels observed in a variety of filters of the infrared (IR) channel of the Wide-Field Camera 3. These variations appear within an exposure in the F105W and F110W filters and both IR grisms (G102 and G141), with background count rates reaching  $5 \text{ e}^-/\text{s}/\text{pix}$  in extreme cases (c.f. the zodiacal background is typically  $\sim 1 \text{ e}^-/\text{s}/\text{pix}$ ). We use IR spectra from both grisms to identify the source of this excess background to be a strong, spatially-diffuse, emission line at  $10,830 \text{ \AA}$  from metastable helium atoms in the solar-illuminated upper atmosphere. The He background contribution is negligible in Earth's shadow but increases sharply when the telescope is outside of the shadow. The He background increases with decreasing limb angle but can also be significant even high ( $>40^\circ$ ) above the Earth limb, affecting, to variable extent, a majority of observations that use the spectral elements sensitive to the feature.*

---

## 1. Introduction

The Wide-Field Camera 3 instrument, the WFC3/IR channel was designed to be background-noise limited for modest exposure times in the broad-band filters (cf. 220–420 seconds; see Table 7.11 of the WFC3 Instrument Handbook v6.0, “IHB”; Dressel et al. 2014). In the space environment, the IR background is a combination of Earth glow, zodiacal light, and thermal emission from the telescope itself. Scattered-light Earth glow is seen with increasing intensity at decreasing target angles above the bright earth limb (Giavalisco et al. 2002). The intensity of the zodiacal light depends on the ecliptic latitude and the target-to-sun angle of a particular observation (see Fig. 9.2 of the IHB). The thermal background is highest

in the reddest filters, but is always secondary to the other background sources due to the long-wavelength cutoff at  $1.7\ \mu\text{m}$ . The WFC3 exposure time calculator (ETC) provides a quantitative estimate of these backgrounds as a function of filter, target coordinates and observation epoch (i.e., target angle to Sun).<sup>1</sup>

For certain *HST* orientations, irregular and time-variable backgrounds have been observed in the IR channel. The strongest of these is an enhancement of the left-most  $\sim 200$  columns of the detector that is likely caused by scattered Earth light reaching the detector through an unintended path through the optics (see Fig. 6.17 of the WFC3 Data Handbook; see also Hilbert & McCullough 2009). This effect will not be discussed further here.

Variations in the background within an orbit timescale can be seen in some of the broad-band filters and with the grisms. Brammer et al. (2012) noted that the G141 grism backgrounds could vary significantly in both 2D structure and intensity within a single orbit. Numerous recent published works have noted strong temporal variations within single exposures in a variety of WFC3/IR filters and grisms (Coe et al. 2013; Koekemoer et al. 2013; Newman et al. 2013).<sup>2</sup> The `calwf3` pipeline assumes constant count rates throughout an exposure in order to flag cosmic rays and bad pixels; some of the background variations seen by Coe et al. and Koekemoer et al. were strong enough that a large fraction of the entire detector was flagged as cosmic rays by `calwf3`, resulting in significantly non-Gaussian noise of the FLT pipeline products.

The WFC3/IR detector is read out in non-destructive MULTIACCUM timing sequences that store the cumulative counts over a number of time steps within a particular exposure. For example, an exposure with the commonly-used SPARS100 sequence could store up to 15 reads in 100 sec intervals for a total of 1402.9 sec (the first read in all of the MULTIACCUM sequences is 2.93 sec; see Chapter 7 of the IHB). Thus, the background count rate (as well as that of an astronomical source) can be sampled within an exposure at a rate determined by the timing sequence used.

In Fig. 1 we show the median count rate per pixel per read for exposures/visits in three IR broad-band filters and both IR grisms. All of the visits shown were selected to have similar orbit+target characteristics: start off in the Earth shadow, “transit” high above the dark Earth limb, and finish the orbit near the  $20^\circ$  bright Earth limb avoidance limit. As in the published results mentioned above, the example exposures show significant enhancements of the background count rate at the end of the orbit in the blue F105W filter and both IR grisms. The deviations from a constant count rate at the level predicted for the zodiacal light can begin at angles  $> 50^\circ$  above the dark Earth limb  $\sim 10$  minutes before the limb is illuminated. The cause of these background variations and strategies for mitigating their effects in data analysis are investigated below.

## 2. Data

In order to study exposures that sample a significant portion of an orbit, we obtain from the MAST archive all public visits<sup>3</sup> with exposure times longer than 600 sec for the F105W

<sup>1</sup>Following the language of the *HST* ETCs and instrument handbooks, throughout we denote as “backgrounds” sources of diffuse light that are explicitly *foregrounds* to (most) astronomical sources.

<sup>2</sup>The time-variable backgrounds in F105W were also noted in recent observations of the *HST* Frontier Fields program; see Koekemoer et al. 2014.

<sup>3</sup>as of Jan. 6, 2014.

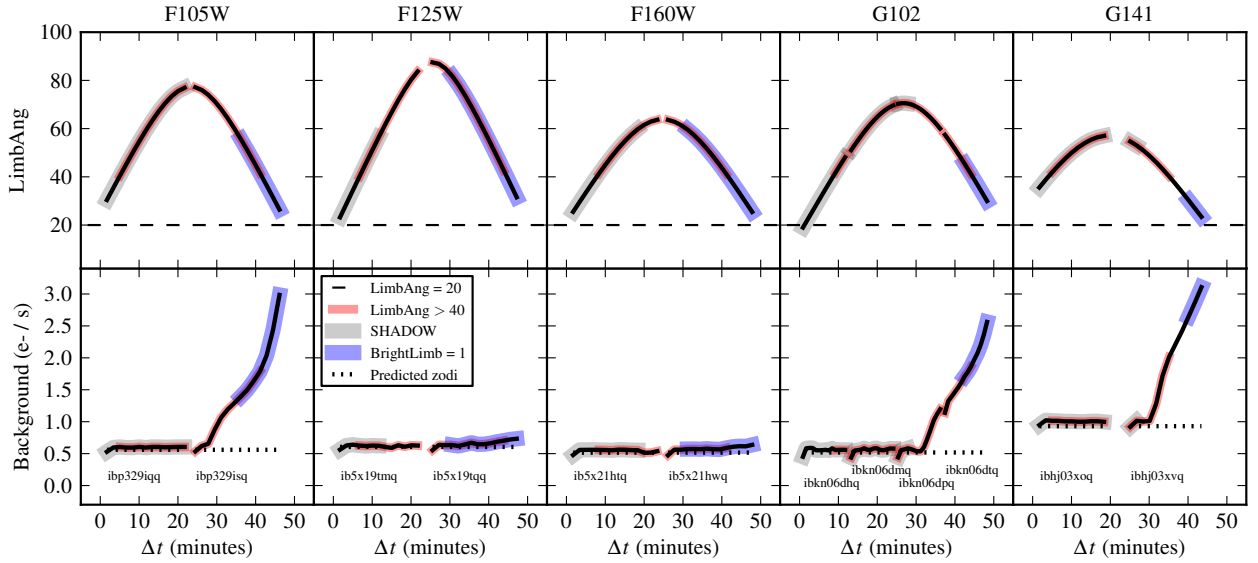


Fig. 1.— *Top panels:* Variation of Earth limb angle through an orbit for demonstrative exposures. The curves are colored following the labels in the legend. The limb angle (“LimbAng”) and limb illumination (“BrightLimb”) are taken from the time sequence and the SHADOW condition is estimated from the SHADOWENT and SHADOWENT keywords of the `jit` files. *Bottom panels:* Variation of the background count rate throughout an orbit for specific WFC3/IR filters and grisms. The predicted background level from the Synphot/ETC zodiacal model is shown in the dotted line. **The F105W, G102 and G141 spectral elements can show strong increases in the background even  $> 40^\circ$  above a dark Earth limb.**

filter. For the more commonly used F125W filter, we limit the search to exposures longer than 1200 sec. For the G102 and G141 grisms, we obtain all of the public full-frame exposures of non-crowded fields<sup>4</sup>. These searches result in 1083 exposures in F105W, 948 in F125W, 1125 in G102, and 1754 in G141.

For every exposure in a defined association (some single orphan exposures that met the search criteria but are not assigned an association are ignored), we measure the median flux of the central  $400 \times 400$  pixels of each of NSAMP reads from the `raw` files to generate tracks like those plotted in Fig. 1<sup>5</sup>. The counts of read  $n$  is simply the difference of the  $[\text{SCI}, n] - [\text{SCI}, n + 1]$  extensions of the `raw` files, which we convert to  $e^-/\text{s}$  assuming a single gain of  $2.5 e^-/\text{DN}$  for all amplifiers and neglecting bias drift, linearity and flat-field corrections. The errors of these simplifications are small compared to the effects seen in Fig. 1 and below. The orbital parameters (angles, satellite subpoint, etc.) are taken from the `jit`, `jif`, and `spt` files when available and computed from header and jitter file values with the `pyEphem` ephemeris software as necessary. We analyze a total  $\sim 10,000$  reads for each of the broad-band filters and the G102 grism and nearly 18,000 reads for G141.

<sup>4</sup>Program IDs 11359, 11600, 12099, 12461, 11696, 12283, 12568, 12902, 13352, 13517, 11597, 12203, 12177, 12328, 11648, 12927, 12547, 12190, 12471, 12330, 12970.

<sup>5</sup>The same information can be extracted from the `ima` pipeline products.

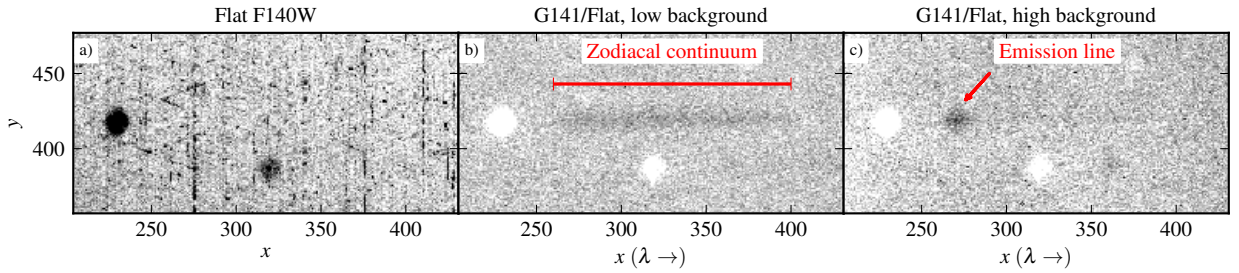


Fig. 2.— *a)* Cutout of the F140W flat-field (PFL) calibration image, showing two “IR blobs” at image coordinates (228, 418) and (315, 386). *b)* Masked and stacked G141 images with relatively low background levels. The G141 images were divided by the F140W flat to remove the pixel-to-pixel variations apparent in (*a*). The blobs from (*a*) now show up as positive features due to the division by the flat. Because the blobs are near the telescope’s focus on the channel select mechanism, their spatial regions of decreased sensitivity are dispersed by the grism resulting in the first order continuum spectrum of the zodiacal background light. *c)* Same as (*b*) but for exposures with high observed background levels. For these images the background spectrum appears to be dominated by an emission line.

### 3. Identification of the time-variable background source

For the grisms, a given pixel sees background flux from overlapping first order spectra of nearby pixels and overlapping spectral orders from more distant pixels. For spatially uniform background sources like the zodiacal light, this results in an approximately uniform background in the grism image, with differences near the  $x$  edges of the detector resulting from differing contributions of overlapping grism orders.

The WFC3/IR channel is affected by “IR Blobs” (Pirzkal et al. 2010, 2012) that are caused by particles on the channel select mechanism that result in dark spots of decreased sensitivity imaged upon the detector and easily seen in the imaging flat-fields (Fig. 2a). In the case of the grisms, the presence of the IR blobs in front of the grism elements in the filter wheel causes slight depressions in the uniform background that are then dispersed, resulting in “negative” spectra with roughly the same contrast as the blobs in the imaging flats. The relatively flat zodiacal continuum spectrum results in elongated first order spectra clearly visible in “master sky” images created by averaging many on-sky grism exposures with astronomical sources masked (Fig. 2; see also Kuemmel et al. 2011; Pirzkal et al. 2011; Brammer et al. 2012).

In many grism exposures with high background levels, the blob spectra appear as compact depressions offset from the nominal positions of the blobs in the imaging filters. This was noticed in grism spectra of the 3D-HST Treasury program by Brammer et al. (2012), who noted that the compact blob spectra in these cases were likely the result of the background being dominated by an emission line component, rather than the usual zodiacal continuum. Fig. 2 shows an example of a flat-field blob and “master sky” images showing the zodiacal continuum (2b) and emission-line (2c) blob spectra taken from Brammer et al. (2012).

Just like the wavelengths of emission lines in grism spectra of galaxies can be measured,

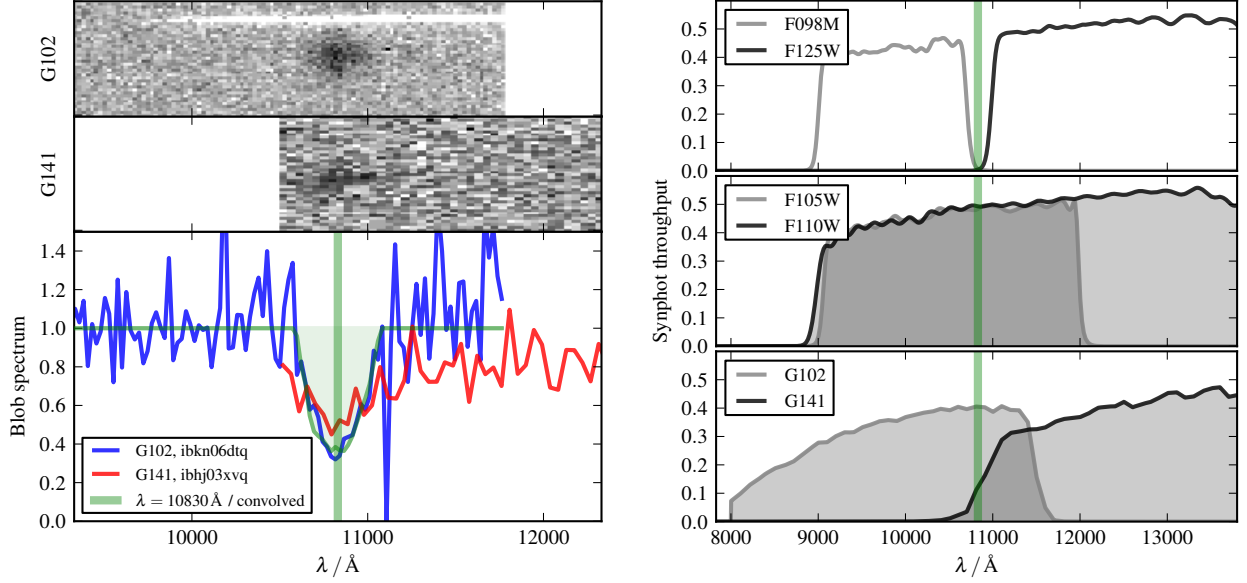


Fig. 3.— *Left panels:* Wavelength-calibrated G102 and G141 spectra of the IR blob at (228,418) from two individual exposures that show the compact feature from Fig. 2c. The feature is at the same observed wavelength in both grisms with  $\lambda = 10,830 \text{ \AA}$ . The green curve and shaded region show the predicted shape of the G102 feature for an unresolved line convolved with the IR blob morphology from the F105W flat field image, which agrees with the observed line shape (blue curve). *Right panels:* Synphot throughput curves of broad WFC3/IR filters and grisms sensitive near  $10,830 \text{ \AA}$ . The F098M and F125W filters just miss the line, while it is near the peak sensitivity of the F105W and F110W filters and the G102 grism and at  $\sim 20\%$  of the peak sensitivity of the G141 grism.

the offset of the dispersed blob with respect to the blob's position in imaging filters indicates the wavelength of the background emission line feature. In Fig. 3 we show spectra of the darkest blob at image coordinates  $(x, y) = (228, 418)$  extracted from two FLT frames that show the feature, one with the G102 grism (ibkn06dtq) and the other with the G141 grism (ibhj03xvq). **The blob lines appear in both grisms at  $\lambda = 10,830 \text{ \AA}$ .** Again we note that the spectral feature is an emission line that *appears* in absorption in the grism spectra due to the obscuration of the IR blobs. The lines are spectrally unresolved, with the 2D structure in the grism spectra determined by the 2D morphology of the blobs themselves. The right panels of Fig. 3 show that the F105W and F110W filters and the G102 and G141 grisms are sensitive to the  $10,830 \text{ \AA}$  line, while it falls in the negligible-sensitivity wings of the F098M and F125W filters.

#### 4. The metastable He $10,830 \text{ \AA}$ emission line

We associate the observed emission line in the WFC3/IR grisms at  $10,830 \text{ \AA}$  with a well-known airglow line coming from metastable He ( $2^3S$ ) in the lower exosphere (Shefov 1961; Bishop & Link 1999). Metastable He is produced by photoelectron impact on ground state He and from  $\text{He}^+$  recombination (Waldrop et al. 2005). The  $10,830 \text{ \AA}$  emission line ( $2^3P - 2^3S$ ) is then produced by resonant scattering of solar photons (Bishop & Link 1999).

Ground-based twilight observations find that the zenith line intensity of He 10,830 Å increases with decreasing local solar zenith angle, reaching a peak at twilight solar zenith angles (Bishop & Link 1999) with intensities of order 1 kR<sup>6</sup>. The production rate of metastable He reaches a maximum at altitudes of 500–600 km (Waldrop et al. 2005), coincident with the orbit of *HST*. The lifetime of He(2 <sup>3</sup>S) is 750–1000 s in the upper atmosphere (> 500 km; McElroy 1965). Thus, during the day side portion of its orbit *HST* is flying through a glowing cloud of He atoms that will produce a spatially diffuse emission line background in all directions, similar to the geocoronal Lyman-α and O I emission lines seen at ultraviolet wavelengths (Holland et al. 2014; §6.5.2).

#### 4.1. Strength of the He 10,830 Å line seen by *HST*

We can use F105W (or F110W) exposures, as well as grism images, to analyze how the strength of the line depends on orbital and target viewing conditions. The source and emission mechanism of the He 10,830 Å described above suggest that the line should be present essentially whenever the spacecraft is flying through atmosphere illuminated by sunlight, possibly with enhancements seen in local twilight when the spacecraft enters or leaves the Earth shadow.

##### F105W

In Fig. 4 we show “excess background” tracks computed as in Fig. 1 and now plotted against the solar hour angle (SHA) of the location on the surface of the Earth directly below the spacecraft, the “subpoint”, at the time of observation. This parameter is directly related to the solar zenith distance, with some secondary dependence on *HST*’s subpoint latitude, but the SHA provides the additional benefit of clearly differentiating between when the spacecraft leaves or enters Earth’s shadow. It is immediately clear from Fig. 4 that the background excess follows the expectations for the 10,830 Å line: the excess over the nominal zodiacal light is negligible inside the Earth shadow and increases dramatically when the atmosphere around the spacecraft is illuminated with sunlight.

At a given SHA, the excess background is strongly correlated with the target-to-limb angle, with the excess increasing as the target gets closer to the limb. It is worth noting again, as in Fig. 1, that the background is elevated even when the limb itself is dark and, furthermore, that significantly elevated backgrounds are seen at large limb angles > 50°. The background excesses for observations approaching zenith are relatively minor, while observations closer to the limb can have more than 4 e<sup>−</sup>/s/pix of additional background over the zodiacal light. In the case of imaging filters such as F105W, every pixel of the detector sees the background line and therefore the average flux across the image provides a measure of the flux of the line. With PySynphot we estimate for the He 10,830 Å line,

$$1 \text{ e}^-/\text{s}/\text{pix} [\text{F105W}] \approx 1.5 \text{ kR}.$$

The average 10,830 Å intensities in Fig. 4 are roughly consistent with those seen from the ground in twilight (~1 kR). The excess during dusk twilight, which will occur in the beginning of an orbit, appears to be somewhat lower than the average seen at dawn twilight, which

---

<sup>6</sup>1 Rayleigh =  $\frac{10^6}{4\pi}$  photons s<sup>−1</sup> cm<sup>−2</sup> sr<sup>−1</sup> =  $3.7 \times 10^{-14}$  (1 Å/λ) erg s<sup>−1</sup> cm<sup>−2</sup> arcsec<sup>−2</sup>

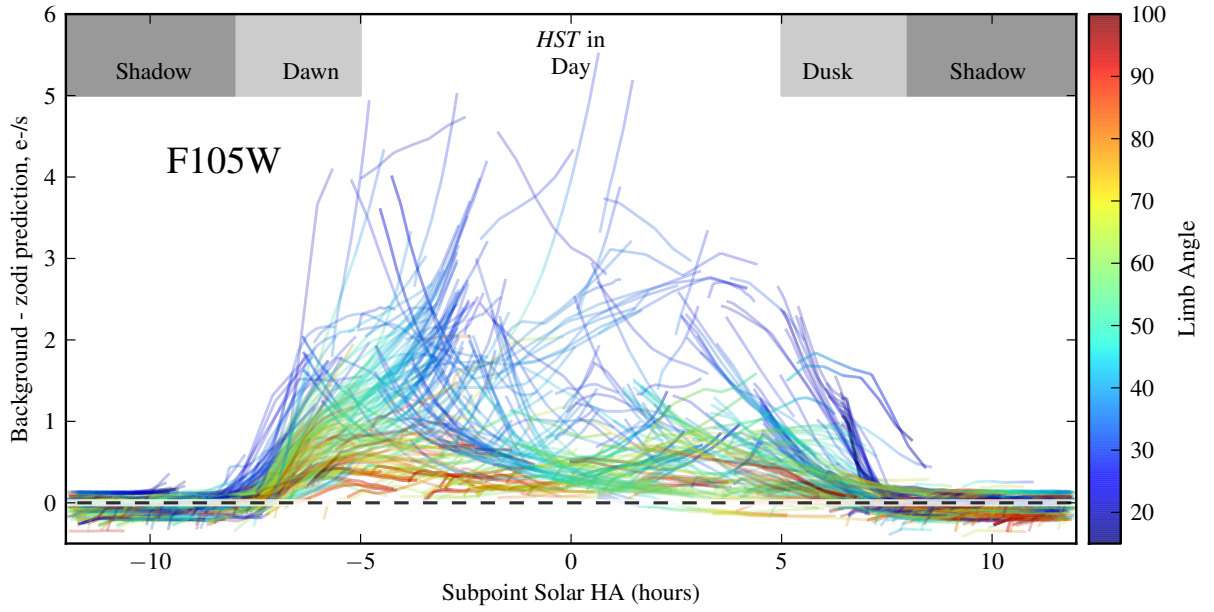


Fig. 4.— Measured excess background in F105W over the zodiacal prediction as a function of the subpoint solar hour angle, which is a proxy for the solar illumination of the atmosphere around the telescope. Each of 1083 GO exposures has a track on this plot computed like those in Fig. 1, with the line segments colored by the target-to-limb angle of each read. Note that the track of a given exposure moves left to right in this figure as the observatory moves from west to east.

will occur at the end of an orbit as the spacecraft orbits from west to east. This could be explained by the fact that the telescope is typically looking East towards the shadow during local dusk twilight with the solar zenith angle increasing along the sightline.

### F125W

In Fig. 5 we show similar background excess tracks as a function of SHA for F125W. As the F125W filter has very low sensitivity at  $10,830 \text{ \AA}$ , we do not expect the He line to contribute significantly to the background seen in that filter, even on the day side of the orbit. Indeed we see little excess for F125W at  $|\text{SHA}| < 8$  hours. There are a few tracks reaching an excess of  $\lesssim 0.4 \text{ e}^-/\text{s}/\text{pix}$ , consistent with an increase in the normal scattered Earth glow at low bright Earth limb angles  $20\text{--}30^\circ$ . There are a few outlier tracks at a wide range of limb angles with a background excess of  $0.5\text{--}1.5 \text{ e}^-/\text{s}/\text{pix}$ . These few observations<sup>7</sup> were taken near the sun angle avoidance limit ( $\sim 50^\circ$ ) and at low ecliptic latitudes ( $< \pm 20^\circ$ ) so it may be that the zodiacal model is inaccurate in these cases.

### G102 and G141 grisms

Figs. 6 and 7 show the background tracks for the G102 and G141 grisms, respectively. Because  $10,830 \text{ \AA}$  is near the peak throughput of the G102 grism, it is strongly affected by

<sup>7</sup>Visits `ibsvb1`, `ibgg40`, and `ibgg41`



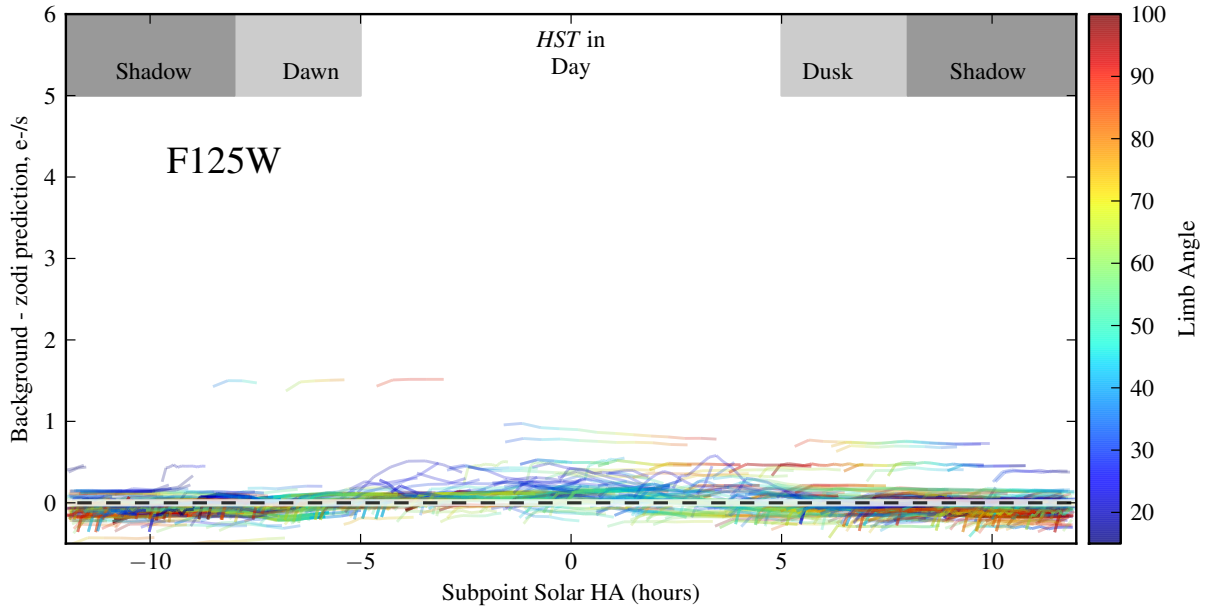


Fig. 5.— Same as Fig. 4 for the F125W filter, which is not sensitive to the 10,830 Å line.

the line. The most extreme G102 tracks reach intensities of 9 kR and trace out a threshold consistent with having the strongest 10,830 Å intensity in twilight and a suppression in the middle of the day. At 10,830 Å the G141 grism has only  $\sim 30\%$  of the throughput of the G102 grism, so it is not as strongly affected by the atmospheric line relative to the zodiacal continuum.

In the case of the grisms, the 2D structure of the background across the WFC3/IR image varies with the spectrum of the line, along with the small-scale changes shown in Fig. 2. This complicates the background subtraction necessary for the analysis of the grism spectra. However, the 10,830 Å line identified here is likely the primary driver of the background variations noted by Brammer et al. (2012) (see their Fig. 4), so new master sky background images constructed now with the knowledge of the strong background line could improve the grism background subtraction significantly. These master sky images will be described in a separate forthcoming ISR.

#### 4.2. Variation with the solar activity cycle

Waldrop et al. (2005) show that the production of metastable He has some dependence on the level of solar activity, with an increased production of metastable He from  $\text{He}^+$  recombination at higher solar activity levels. We evaluate the dependence of the 10,830 Å line strength on solar activity by isolating reads obtained during orbital daytime ( $|\text{SHA}| < 8$  hours). The background excess for these reads is plotted against the (bright) Earth limb angle in Fig. 8. At constant limb angle, the solar activity parameterized by the solar 10.7 cm flux (F10.7; Covington 1969) is in fact correlated with elevated 10,830 Å background levels. Along with the general correlation, the most extreme G102 tracks in Fig. 6 reaching 9 kR are in fact found to correspond to peaks in the F10.7 index with  $\text{F10.7} > 180 \text{ sfu}^8$ . We are currently at

<sup>8</sup>1 sfu =  $10^{-22} \text{ W m}^{-2} \text{ Hz}^{-1}$ .



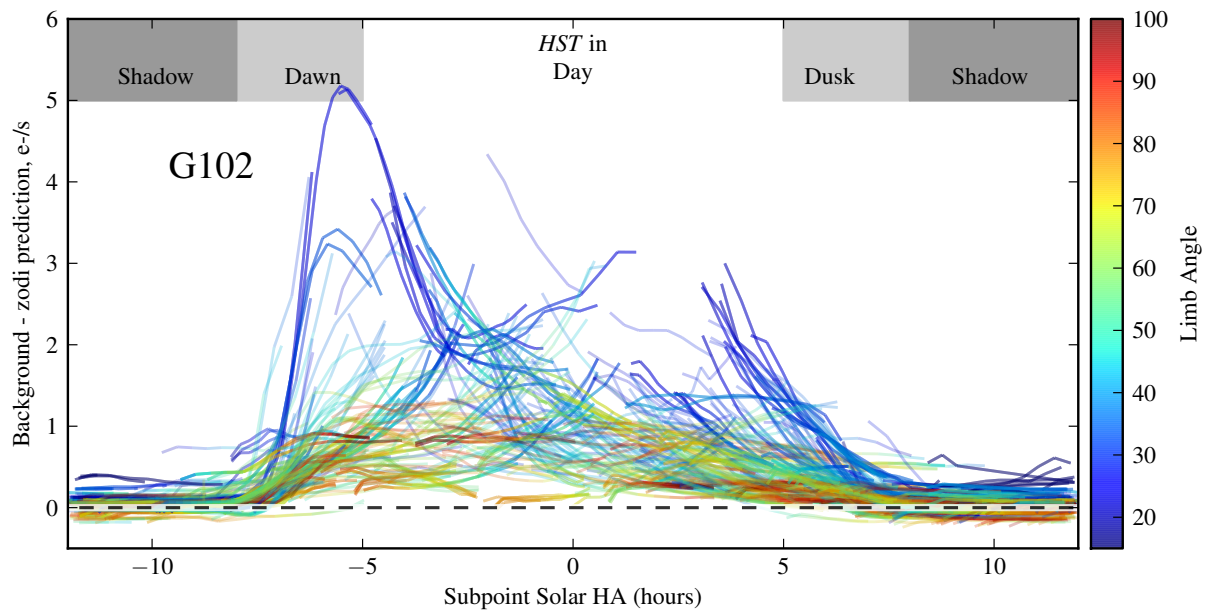


Fig. 6.— Same as Fig. 4 for the G102 grism.

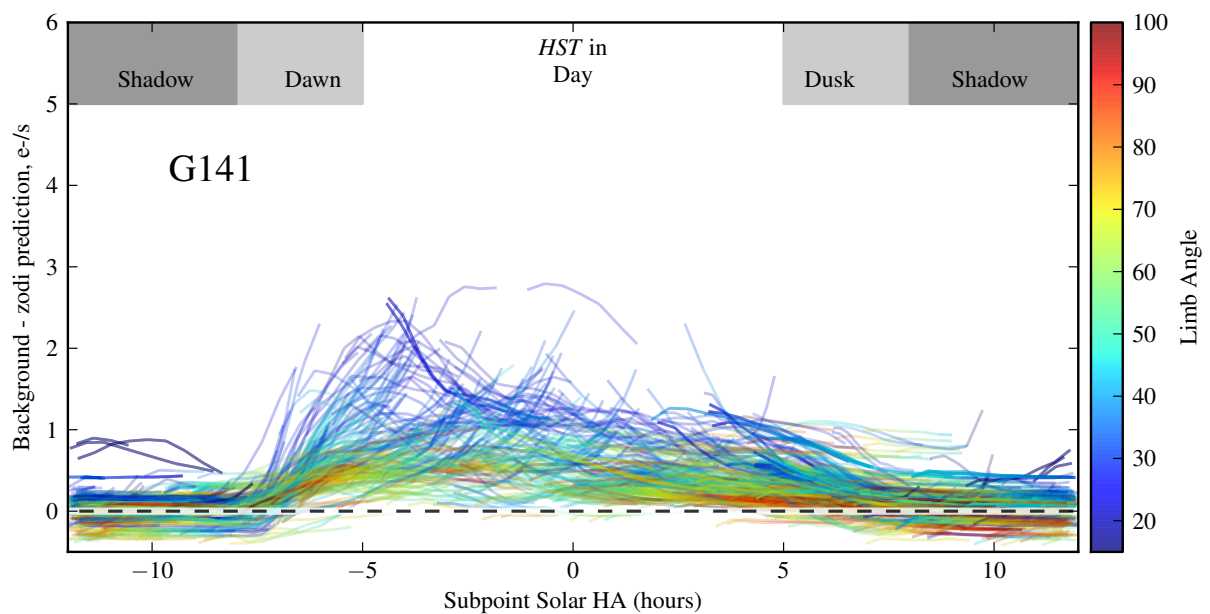


Fig. 7.— Same as Fig. 4 for the G141 grism. The dark blue curves showing an excess of  $\sim 1 e^-/s/pix$  at  $|HA| > 9$  hours are grazing observations at dark Earth limb angles  $< 10^\circ$  of southerly targets.

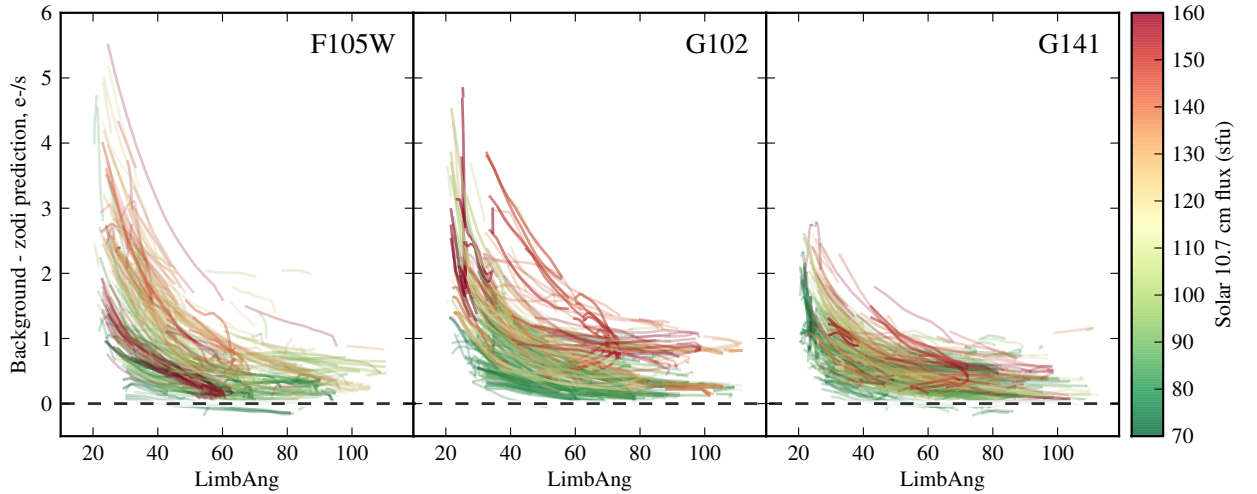


Fig. 8.— Background excess as a function of Earth limb angle for dayside exposures (solar HA  $< \pm 5$  hours). The tracks are colored according to the daily F10.7 solar activity index (Covington 1969) obtained from <http://www.spaceweather.ca/solarflux/sx-eng.php> and plotted in solar flux units (sfu; see footnote below).

the maximum of the solar activity cycle (2012–2014) so this could continue to cause further elevated background levels in the filters and grisms sensitive to the 10,830 Å line.

#### 4.3. Effect on observing efficiency

The tracks in Figs. 4–7 show that the excess backgrounds from the 10,830 Å can be quite bright; however, they do not indicate the specific fraction of reads and exposures affected by the line in the filters and grisms sensitive to it. In Fig. 9 we show the distribution of the *ratio* of the observed background to the nominal zodiacal light prediction at the target coordinates and observing epoch, which we denote as  $X$ .<sup>9</sup> For background-limited observations, the sensitivity of exposures with elevated background levels is decreased by a factor of  $1/\sqrt{X}$ . The fraction of reads with  $X > 2$  (a 40% decrease in sensitivity) is indicated in the figure: this fraction is 7% for the G141 grism with lower throughput at the wavelength of the He line and reaches nearly 20% of for F105W and G102. To reach a given sensitivity in the presence of backgrounds elevated by a factor of  $X$ , one must integrate a factor of  $X$  longer, resulting in an overall decrease of the observatory efficiency of a factor of  $1/X$  (in the affected filters and grisms). We indicate the integrated value over all  $N$  individual reads of this effective efficiency in the figure, with

$$eff. = \frac{1}{N} \sum \frac{1}{X}.$$

The 10,830 Å emission line background reduces the observing efficiency in the affected filters and grisms by nearly 25% for the ensemble of observations shown.

In Fig. 10 we explore the tradeoffs between using the F105W and F110W filters that

<sup>9</sup>The previous figures show the *difference* of these quantities providing a quantitative measure of the intensity of the line.

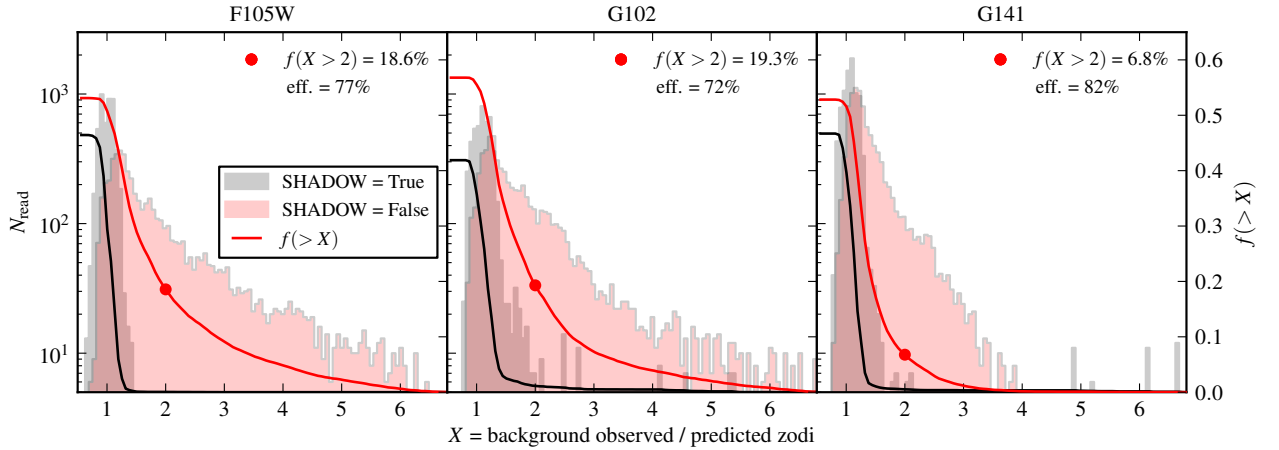


Fig. 9.— Incidence of excess backgrounds caused by the He 10,830 Å line. The distributions shown are the ratio  $X$  of the observed background to that predicted from the zodiacal light model for the *individual reads* of  $>1000$  exposures considered for each spectral element. The histograms are separated between reads that occurred while the telescope was inside (black) and outside (red) the Earth’s shadow. The solid red and black curves show the cumulative distributions  $f(>X)$ , with respect to *all* reads.

are sensitive to the 10,830 Å line and the F098M filter, which is not. The left panels of Fig. 10 show a sensitivity analysis of the two F105W exposures also shown in Fig. 1, where the background sharply increased during the second exposure of the orbit as a result of the 10,830 Å line. Using PySynphot we assume a source spectrum flat in AB magnitudes and include error terms identical to those used by the ETC. The solid curves show the expected sensitivities for a constant zodiacal background as observed. The observed and inferred sensitivities in the presence of the 10,830 Å line are shown in the dashed lines, which peel away from the optimal “ $\sqrt{t}$ ” curves at the end of the second exposure (the glitch in the middle of the curves is the read noise associated with having a second exposure in the orbit).

In the right panel of Fig. 10 we show an aggregate analysis for 315 archival F105W associations also analyzed in the sections above, where the horizontal axis is the ratio of the observed F105W sensitivity in the presence of the 10,830 Å line compared to that inferred for F098M with pure zodiacal backgrounds. This is the ratio of the rightmost points of the dotted green curve and solid blue curves in the left panel of Fig. 10 now shown for many additional visits. Even given the significantly increased 10,830 Å backgrounds as shown in the tracks in Fig. 1, we find that the broader F105W is still more sensitive than F098M that is not sensitive to the additional background (the very wide F110W is more sensitive still with or without the 10,830 Å background). We note that these conclusions depend somewhat on the assumed source spectrum, though they are in fact stronger for sources with redder SEDs (e.g., most galaxies). Nevertheless, we caution users that ETC S/N estimates for the F105W and F110W filters (and to some extent the IR grisms) will be optimistic by average factors of 10% and 7%, respectively, given the analysis shown in Fig. 10.

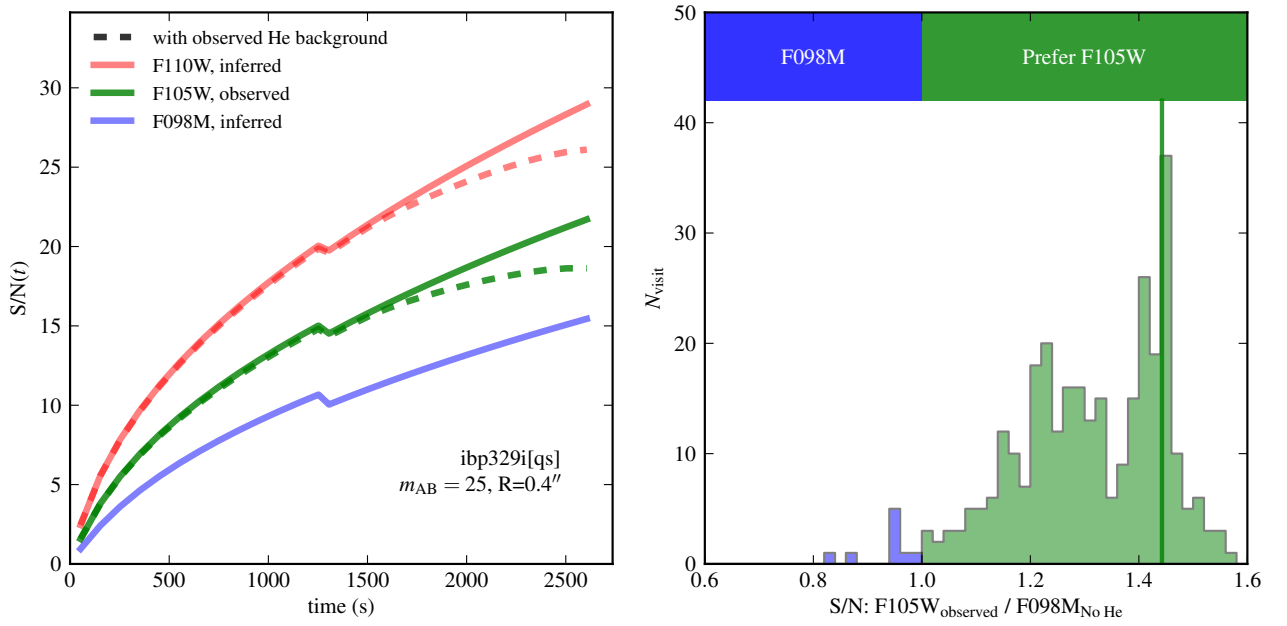


Fig. 10.— *left*: Signal-to-Noise as a function of exposure time through one two-exposure visit (the same F105W exposures shown in Fig. 1), assuming a source spectrum flat in AB magnitudes with  $m = 25$ . With the elevated background at the end of the visit from of the 10,830 Å line, the overall sensitivity of the visit is decreased by 17% (green dashed line). However, the obtained sensitivity is still greater than it would have been had the narrower F098M filter been employed (blue line) in place of F105W. *right*: Similar sensitivity analysis for 315 F105W associations covering more than 300 orbits. The expected sensitivity ratio of the F105W and F098M filters given the broader width of the redder passband is shown by the vertical green line. While the derived sensitivity ratios in the presence of the 10,830 Å line as observed are usually less than this ideal value, they are almost always greater than unity, i.e., F105W is still more sensitive than F098M for a given exposure time.

## 5. Mitigation strategies

The following section discusses strategies for mitigating the effect of the increased and time-variable backgrounds caused by the 10,830 Å line. For the future, we are investigating whether additional scheduling constraints can be developed that would decrease the incidence of elevated backgrounds from 10,830 Å line without significantly decreasing the overall scheduling efficiency of the observatory. As is clear from Figs. 4–7, the APT SHADOW constraint would effectively eliminate background contamination from the 10,830 Å line, but at the significant cost of much shorter orbital durations ( $\sim 25$  minutes). Even in the presence of rapidly a increasing (or decreasing) background, we find that it is preferable to “leave the shutter open”, that is, the source  $S/N$  still increases with exposure time but at a rate slower than  $\sqrt{t}$  (see Fig. 10). We note that the LOW-SKY APT flag accounts only for zodiacal light and limb angle, so it does not eliminate the possibility of an increased 10,830 Å background well above the limb (Fig. 1).

The following items discuss strategies for processing observations already in the archive:

- For exposures with strongly variable backgrounds that result in many pixels flagged as cosmic rays and non-Gaussian noise in the `flt` images, one can rerun `calwf3` setting `CRCORR=OMIT` to turn off the linear-ramp fitting and cosmic ray rejection. This technique loses some dynamic range for sources that saturate during the exposure and whose flux would normally be recovered from the unsaturated part of the ramp. Additionally the `flt` products produced this way will contain all of the incident cosmic rays, though these can often be effectively identified given a sufficient number of dithered exposures with software such as AstroDrizzle.
- Some groups, such as the HST Frontier Fields team at STScI, have developed techniques to fit non-linear ramps to the pixel count rates, which would account for the variable 10,830 Å background count rates such as those shown in Fig. 1. The WFC3 team is investigating the feasibility of implementing this capability in `calwf3`.
- In the case of the IR grisms, the Frontier-Fields style non-linear ramp fitting is complicated by the fact that the zodiacal and 10,830 Å backgrounds result in distinct two-dimensional structure in the background, including structure at high spatial frequencies of order of a few pixels in the emission line blobs (Fig. 2) and in the bands of overlapping grism orders at the left and right ( $x$ ) edges of the detector. Brammer et al. (2012) noted the need for a variety of grism “master sky” images to explain the observed variation in the background structure, though they were ignorant of the 10,830 Å line as the primary driver of the variations. We are developing an improved set of master sky images now with the knowledge of the 10,830 Å line that possibly could be subtracted from each individual read depending on the relative contributions of the zodiacal and 10,830 Å backgrounds to that read (Brammer et al., ISR in prep).

## 6. Summary

We identify an emission line at 10,830 Å from metastable helium in the Earth’s upper atmosphere that can increase the IR background levels by as much as a factor of six over the nominal zodiacal background. The line is typically not seen while the observatory is in the Earth shadow. We conclude that it is a spatially-diffuse source local to the telescope during the portions of the orbit where HST and its local atmosphere are illuminated by sunlight. At a given target-to-limb angle out of the Earth shadow, there is some correlation of the excess 10,830 Å background with solar activity, with higher background levels at times of increased activity.

As most WFC3/IR observations are background-limited, excess background from the 10,830 Å line decreases the sensitivity of a given exposure and decreases the observing efficiency of the observatory on the whole (in the affected filters and grisms). Furthermore, the simple “up-the-ramp” fitting performed by the `calwf3` pipeline can fail in the presence of variable backgrounds *within* an exposure and produce unreliable results. We describe several strategies for accounting for the variable backgrounds in archival observations, the simplest being turning off the cosmic-ray rejection step (`CRCORR`) of `calwf3`. Further work

remains to identify scheduling strategies to reduce the incidence and severity of the excess He 10,830 Å backgrounds.

We would like to thank Knox Long for reviewing and providing helpful comments on this manuscript.

## References

- Bishop, J. & Link, R., 1999, *J. Geophys. Res.*, **104**, 17157 [ADS]
- Brammer, G. B., et al., 2012, *ApJS*, **200**, 13 [ADS]
- Coe, D., et al., 2013, *ApJ*, **762**, 32 [ADS]
- Covington, A. M., 1969, *JRASC*, **63**, 125 [ADS]
- Dressel, L., et al., 2014 “Wide Field Camera 3 Instrument Handbook, Version 6.0” [URL]
- Giavalisco, M., et al., 2002, WFC3 ISR 2002-12, “New Estimates of the Sky Background for the HST Exposure Time Calculator” [PDF]
- Hilbert, B. & McCullough, P.R.M., 2009, WFC3 ISR 2009-21, “WFC3 SMOV Results: IR Channel Dark Current, Readnoise, and Background Signal” [PDF]
- Holland, S. T., et al. 2014, “Cosmic Origins Spectrograph Instrument Handbook, Version 6.0” [PDF]
- Koekemoer, A. M., et al., 2013, *ApJS*, **209**, 3 [ADS]
- Koekemoer, A. M., et al., 2014, MAST Frontier Fields README v1.0, [http://archive.stsci.edu/pub/hlsp/frontier/abell12744/images/hst/v1.0/hlsp\\_frontier\\_hst\\_wfc3-acs\\_abell12744\\_v1.0\\_readme.pdf](http://archive.stsci.edu/pub/hlsp/frontier/abell12744/images/hst/v1.0/hlsp_frontier_hst_wfc3-acs_abell12744_v1.0_readme.pdf)
- Kockarts, G., 1973, *Space Sci. Rev.*, **14**, 723 [ADS]
- Kuemmel, M., et al., 2011, WFC3 ISR 2011-01, “Master Sky Images for the WFC3 G102 and G141 Grisms” [PDF]
- McElroy, M. B., 1965, *Planet. Space Sci.*, **13**, 403 [ADS]
- Newman, A. B., et al., 2013, *ApJ*-submitted, arXiv/1310.6754 [ADS]
- Pirzkal, N., et al., 2010, WFC3 ISR 2010-06, “The WFC3 IR Blobs” [PDF]
- Pirzkal, N., et al., 2011, WFC3 ISR 2011-11, “Sky Flats: Generating Improved WFC3 IR Flat-fields” [PDF]
- Pirzkal, N. & Hilbert, B., 2012, WFC3 ISR 2012-15, “The WFC3 IR Blobs Monitoring” [PDF]
- Shefov, N. N., 1963, *Planet. Space Sci.*, **10**, 73 [ADS]
- Waldrup, L. S., et al., 2005, *J. Geophys. Res.*, **110**, 8304 [ADS]